To cite this version:

Murai, Yuichi and Tasaka, Yuji and Oishi, Yoshihiko and Ern, Patricia Bubble fragmentation dynamics in a subsonic Venturi tube for the design of a compact microbubble generator. (2021) International Journal of Multiphase Flow, 139. 103645. ISSN 0301-9322

Bubble fragmentation dynamics in a subsonic Venturi tube for the design of a compact microbubble generator

Yuichi Murai [a,*], Yuji Tasaka [a], Yoshihiko Oishi [b], Patricia Ern [c]

[a] Laboratory for Flow Control, Faculty of Engineering, Hokkaido University, N13W8, Sapporo, Hokkaido, 060-8628, Japan
[b] Muroran Institute of Technology, Muroran, Hokkaido, 050-8585, Japan
[c] Institut de Mécanique des Fluides de Toulouse, 31400 Toulouse, France

ABSTRACT

Microbubble generators are in wide demand in industry following the discovery of a number of new functions of microbubble mixtures. This paper deals with a Venturi tube microbubble generator in which air bubbles at the inlet are fragmented in the diverging part of the tube. In contrast with past studies, we here regulated the flow subsonic so that fragmentation occurred without the help of pressure shock waves. Counting the microbubbles in image processing, we found that a single bubble fragmented into 20–400 microbubbles depending on the Weber number. The power efficiency is found to range from 30 to 50 percent and insensitive to the liquid viscosity. The mechanism of subsonic fragmentation is elucidated adopting particle tracking velocimetry, in association with a theoretical description of the translational motion and the shape oscillation of the bubble. The key event was found to be the bubble's rapid slip-back in the diverging part of the Venturi tube due to a positive pressure gradient. This provides a function that prevents large bubbles from being released from the subsonic Venturi tube.

1. Introduction

The functions of microbubbles are receiving much attention in the fields of science and engineering. Microbubbles have beneficial properties in water; e.g., rheological, electro-chemical, and biomechanical effects (Agarwal et al., 2011; Terasaka et al., 2011). A representative feature of microbubbles is a high interfacial area concentration. Microbubbles thus promote heat and mass transfer between gas and liquid phases via densely distributed gas–liquid interfaces (Kitagawa and Murai, 2013; Ichikawa et al., 2018). Additionally, the injection of microbubbles into turbulent shear layers suppresses momentum transfer. Progress is now being made in reducing frictional drag through the injection of microbubbles (Hara et al., 2011; Murai, 2014; Park et al., 2019). The use of microbubbles benefits not only the control of fluid properties but also measurement techniques; i.e., microbubbles work as tracers in particle image velocimetry (PIV), acoustic echography, and ultrasonic Doppler velocimetry. Their small size allows microbubbles to follow the liquid flow within certain limits of flow turbulence (Mathai et al., 2016). Moreover, microbubbles hardly coalesce owing to their resistance against deforma-

tion, and they even repulse each other owing to a zeta potential (Usui and Sasaki, 1978; Calgaroto et al., 2014). These properties warrant the use of microbubbles as a flow tracer, avoiding aggregation in flow. In PIV, two additional merits of microbubbles are recognized, i.e., high sphericity for strong surface tension and a brilliant light–scattering property (Cheng et al., 2005; Park et al., 2019). In ultrasound Doppler velocimetry, individual microbubbles strongly reflect pulsed ultrasound owing to the large gap in acoustic impedance at their interfaces (Simpson et al., 1999; Takeda, 2012).

The power efficiency of microbubble generation has not been evaluated in most cases of the applications of microbubbles mentioned above. The total energy balance needs to be assessed for practical use. In large facilities, such as those used for water purification, biochemical reactors, and ship drag reduction, the research and design of microbubble generators currently targets improvements in power performance. Regarding energy, a microbubble generator adopting the depressurization of bubble nuclei requires high thermodynamic power in a pressure vessel (Maeda et al., 2015). Microbubble generators adopting a mechanical shearing device (e.g., Sadatomi et al., 2005) consume power in pumping and shearing the liquid.

A Venturi tube can be used to generate microbubbles in a compact space. The Venturi tube continuously divides bubbles into hundreds of microbubbles downstream. Furthermore, the Venturi

Table 1
Available reports on bubbly flow in Venturi tubes.

Report by	Geometry	Throat size	Throat velocity	Gas injection	Final bubble size
Uesawa et al. (2012)	Axisymmetric	6 mm	10 to 90 m/s	Upstream	30 – 80 μm
Kuroshima et al. (2014)	Rectangular	2 mm	2 to 11 m/s	Upstream	100 – 600 μm
Yin et al. (2015)	Axisymmetric	23 mm	4 to 13 m/s	Throat surface	300 – 1200 μm
Lee et al. (2019)	Axisymmetric	20 -32 mm	2 to 25 m/s	Throat surface	20 – 350 μm
Zhao et al. (2018, 2019)	Rectangular	25 mm	2 to 13 m/s	Throat surface	1000 – 5000 μm
Huang et al. (2019, 2020)	Rectangular	2 mm	6 to 10 m/s	Throat surface	100 – 800 μm
Present study	Axisymmetric	2 mm	7 to 12 m/s	Upstream	50 – 200 μm

tube does not need any mechanical moving parts or ambient pressurizing process. The tube is also used for atomization of droplet in gas flow (Silva et al., 2009). When bubbly two-phase flow passes through the Venturi tube, it readily reaches the speed of sound in bubbly flow (>20 m/s) at the throat part and becomes supersonic in the diverging part (Thang and Davis, 1981). This results in pressure shock waves collapsing the bubbles, the detailed process of which was investigated by Uesawa et al. (2012). Reducing the flow speed to a subsonic level, Yin et al. (2015) measured the sizes of fragmented bubbles produced by an asymmetric Laval nozzle of a Venturi tube at flow speeds of 4 to 13 m/s. They formulated the resultant bubble size as being dependent on the Reynolds number considering that liquid-phase turbulence determines the final bubble size. For a comparable range of the flow speed, Lee et al. (2019) injected bubbles directly at the throat part of a symmetric Venturi tube and found fragmentation promoted by flow separation of the liquid phase at the rear edge of the throat part. Zhao et al. (2018, 2019) and Huang et al. (2019, 2020) injected gas continuously into a rectangular Venturi throat at a speed lower than the speed of sound and found the importance of slipping due to buoyancy in the destabilization of gas–liquid interfaces. In their cases, gas was injected from throat surface and thus shear stress near the wall played major role of fragmentation. Kuroshima et al. (2014) examined bubble fragmentation in a two-dimensional Venturi tube and found reversing water jet inside a bubble during sharp negative acceleration. Table 1 lists comparison of these experimental conditions. In summary, the Venturi tube has several different functions that promote bubble break-up, depending on the flow speed of the liquid phase.

Our study focuses on microbubble generation using an axisymmetric Venturi tube operated within subsonic flow conditions. We expect two advantages from subsonic conditions in engineering applications. One is the suppression of acoustic noise that reduces the signal-to-noise ratio of acoustic echography and ultrasound Doppler velocimetry. Such suppression is possible using subsonic

flow for which there is no volumetric pulsation of bubbles. The other is improved controllability of the bubble size through the tuning of geometric parameters. From an energy perspective, we expect acoustic and thermodynamic loss to be reduced in subsonic operation. In this paper, we investigate experimentally the breeding number of bubble fragmentation in a subsonic Venturi tube. The data are collapsed using a function of the Weber number. The mechanism of bubble fragmentation is then discussed referring to the velocity profiles of liquid and bubbles obtained in particle tracking velocimetry. The final section gives a theoretical description of bubble fragmentation to explain the trend of measurement data and to characterize subsonic bubble fragmentation in a Venturi tube.

2. Experimental Method

2.1. Experimental setup

Figure 1 is a schematic diagram of the main body of the experimental setup. The working fluid is carried by a volumetric displacement pump at a constant flow rate and lead into a Venturi tube. The tube is made from transparent glass and has an inner diameter of $D_{th} = 2$ mm at the throat section with an axial length of 2 mm. The inlet and outlet sections both have a diameter of $D_o = 8$ mm. The converging and diverging parts both have a length of $L = 17.3$ mm, such that the total length of the tube is 36.6 mm. In this configuration, the diverging angle is $\tan^{-1}$ (3.0 / 17.3) = 10 degrees, at which liquid flow undergoes separation (Sparrow et al., 2009). We manufactured such a Venturi tube for two reasons. One is that the flow is controlled to be subsonic, and an asymmetric shape as for a Laval nozzle in the case of adiabatic expansion is thus unnecessary. The other is that we want to create a symmetric pressure profile inside the Venturi tube, with which an asymmetric process associated with the dispersion behavior can be clearly extracted. In our experiment, a single bubble was injected at the
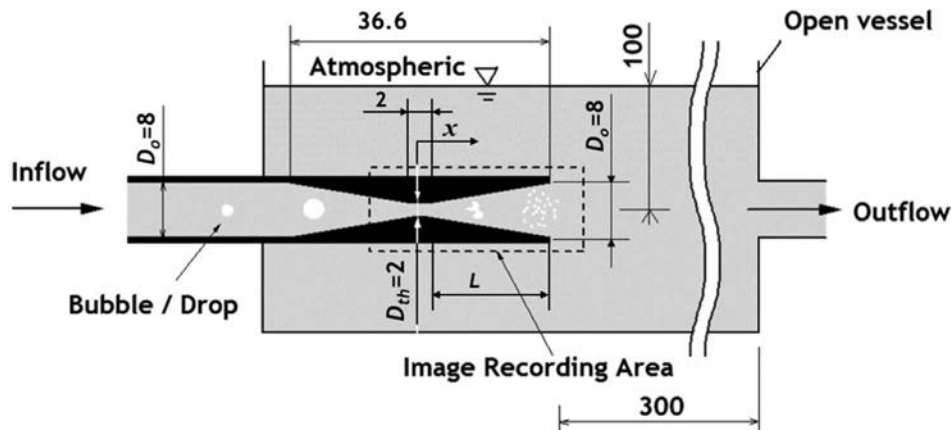

Fig. 1. Schematic diagram of the experimental setup comprising a symmetric Venturi tube with a constant taper angle in an open vessel. A single bubble is released in the upstream part from an injection needle and passes through the throat of the tube to be fragmented in the diverging part.

Table 2
Experimental and photographic conditions.

Flow rate Q [l/min]	1.50, 1.80, 2.10
Reynolds number Re	6.1×10^3 to 23.0×10^3
u_{th} [m/s]	7.9 to 11.5
Frame rate [fps]	8,000
Shutter speed [1/s]	100,000
Focal ratio [-]	5.6
Picture size [pix]	256×1024

Table 3
Properties of glycerol aqueous solutions.

Concentration	[%]	0	10	20	30
Viscosity	[x10^{-3} Pa·s]	1.01	1.31	1.77	2.50
Surface tension	[x10^{-3} N/m]	72.8	72.9	72.4	72.0

upstream position from a small capillary needle. The carrier liquid conveys the bubble into the throat section, where pressure decreases owing to Bernoulli's effect. The bubble breaks up in the downstream diverging part, where there is a large slip from the liquid phase. The downstream liquid containing fragmented bubbles is released into an open vessel.

When changing the liquid, the effect of viscosity is evaluated using the Reynolds number, defined as

$$Re = \frac{u_{th}D_{th}}{\nu}, \qquad u_{th} = Q\left(\frac{1}{4}\pi D_{th}^2\right)^{-1}, \tag{2-1}$$

where ν is the kinematic viscosity of the liquid, u_{th} is the mean velocity of the liquid in the throat section, and Q is the liquid volume flow rate. The experimental ranges for these parameters are summarized in Table 2. We examined four different liquids as the carrier phase; i.e., pure water and 10%, 20%, and 30% glycerol aqueous solutions (see Table 3 for properties). The initial diameter of bubbles at the inlet section ranged from 0.2 to 1.2 mm. The imaging area for measuring bubble fragmentation was set such that it included the throat section and the downstream end of the Venturi tube; the window dimensions were 6.0 mm $\times$ 24.0 mm and 256×1024 pixels, giving a magnification factor of 23 mm/pixel.

Images were recorded by a high-speed digital video camera (Photron, FASTCAM-MAX) at a frame rate of 8000 fps and shutter speed of 10^5 s^{-1}. Other photographic conditions are summarized in Table 2. The interfaces of bubbles were back-lit such that they could be identified as shadows due to differences in the optical refractive index between the two fluids.

Regarding the compressibility of bubbles, we regulate the Mach number as

$$Ma = \frac{u_{th}}{c} < 0.3, \quad c = \min\left\{c_0, \sqrt{\frac{p}{\alpha(1-\alpha)\rho}}\right\}, \tag{2-2}$$

where c is the speed of sound in the bubbly mixture determined by the speed of sound in water c_0, pressure p, density of liquid ρ, and void fraction α. In the case of shallow water, p/ρ is approximately 100 m^2/s^2, yielding the speed of sound in the bubbly mixture as $c = 100$ m/s at $\alpha = 1\%$, $c = 45$ m/s at $\alpha = 5\%$, and $c = 35$ m/s at $\alpha = 10\%$. In all cases, the maximum liquid velocity was restricted as $u_{th} < 12$ m/s; i.e., the subsonic state in gas–liquid two-phase flow.
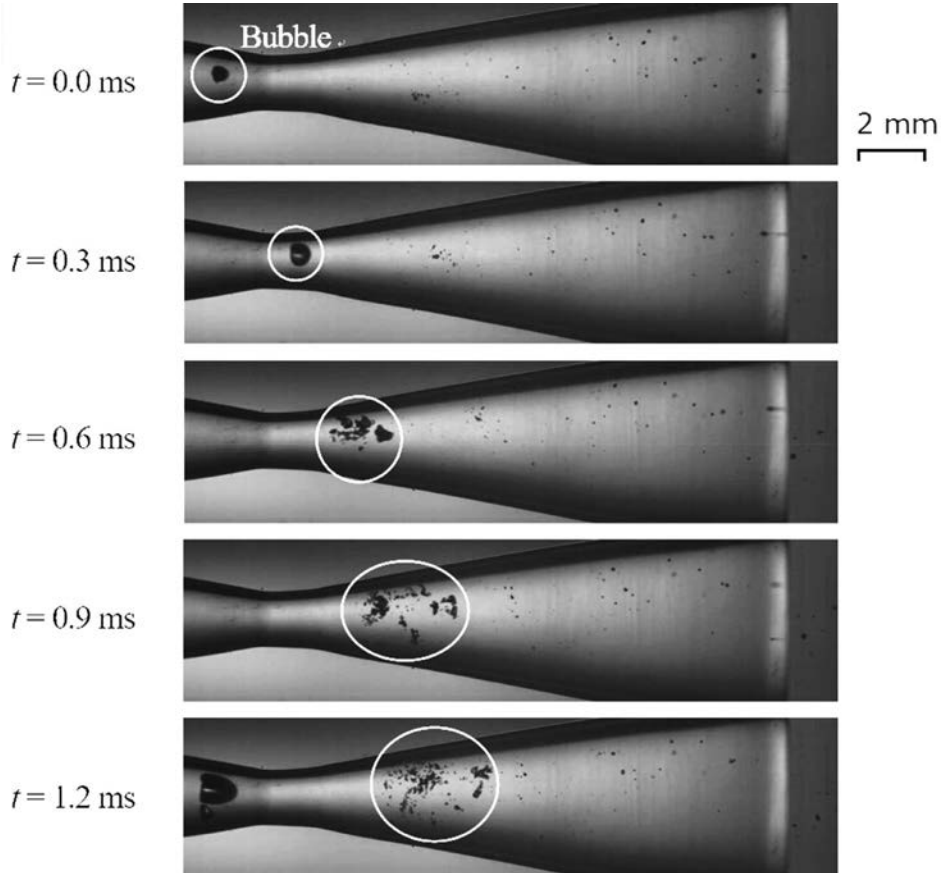

Fig. 2. Consecutive high-speed camera images of bubble fragmentation inside the diverging part for a throat flow velocity of $u_{th} = 8$ m/s, taken as shadow images with backlighting.
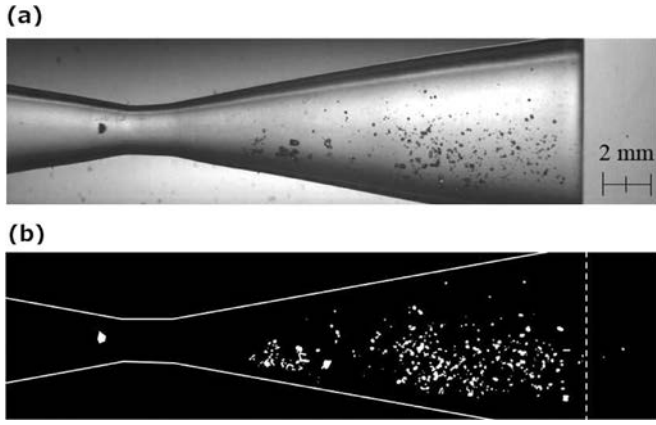
Fig. 3. Image processing in the counting of the number of fragmentated bubbles: (a) original image and (b) binarized image obtained using a threshold with Otsu's maximum cross deviation scheme, allowing counting of the microbubbles.

2.2. Method of image analysis

Figure 2 presents a time sequence of bubble fragmentation in 100% water. The liquid flow rate is $Q = 1.5$ l/min and the liquid velocity at the throat is $u_{th} = 8$ m/s in this case. A bubble having an initial diameter of $d_1 = 0.6$ mm fragmented after passing through the throat. The bubble split into several pieces at $t = 0.6$ ms and became 100 microbubbles at $t = 1.2$ ms. We counted the number of microbubbles through image processing. The image in **Fig. 3**(**a**) was converted to that in **Fig. 3**(**b**) by subtracting the background and thresholding the brightness. The maximum cross deviation scheme (Otsu, 1979) was applied in thresholding the images. This allowed for the maximum number of microbubbles to be captured accurately. Whereas the individual shapes of microbubbles could not be identified due to their small size (<10 mm), the number of microbubbles could be counted. It is noted that the radial position of microbubbles in the image shifts outward owing to the refraction of light at the glass–water interface. Therefore, microbubbles flowing close to the inner wall were not counted; however, these were a small percentage (less than 5%) of the total count. An error of 5% can be regarded as a minor effect because fragmentation occurs in an exponential manner. We also measured the bubble velocity using a PTV algorithm. In PTV, a two-frame nearest neighbor search was conducted for a pair of consecutive images. The maximum measurable range of the velocity was 0 to 15 m/s with a velocity resolution of 0.05 m/s.

In this experiment, the period of the initial bubble injection at the inlet of the Venturi tube was controlled to be sufficiently longer than the time required for the bubble to pass through the tube. This avoided the mixing of microbubbles generated by two initial bubbles.

3. Experimental Results and Discussion

3.1. Performance of bubble fragmentation

We collected data of the performance of bubble fragmentation by injecting bubbles having various initial diameters, d_1. **Figure 4** shows the case for pure water while **Fig. 5** shows that for 30% glycerol aqueous solution. Each plot shows the relation between d_1 and the average diameter of fragmented bubbles d_2. The initial diameter d_1 was measured by image processing for individual bubbles entering the inlet plane of the tube. To obtain d_2, we used a relationship between d_2 and the fragmentation number N, which gives the arithmetic average diameter of the bubbles after fragmenta-
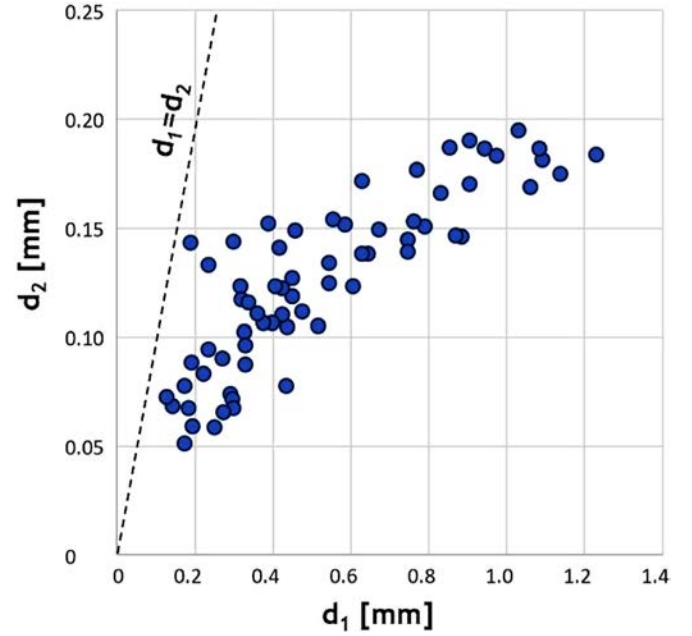

Fig. 4. Relationship between the diameter of the injected bubble d_1 and diameter of the fragmented bubble d_2 in 100% water at a throat flow velocity of $u_{th} = 11.5$ m/s ($Q = 2.10$ l/min), showing positive correlation.
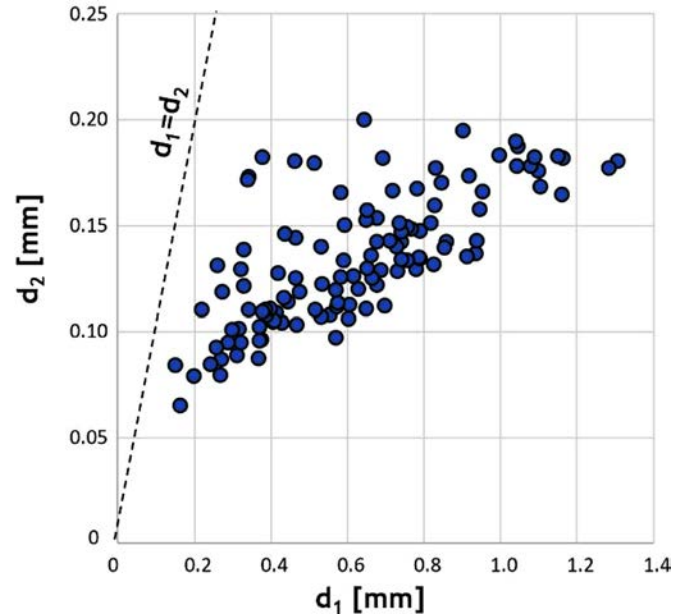

Fig. 5. Relationship between the diameter of the injected bubble and the diameter of the fragmented bubble in 30% glycerol aqueous solution, which has a viscosity 2.5 times that of water, measured at a throat flow velocity of $u_{th} = 11.5$ m/s ($Q = 2.10$ l/min).

tion:

$$\frac{1}{6}\pi d_1{}^3 = N \cdot \frac{1}{6}\pi d_2{}^3, \;\; \rightarrow \;\; d_2 = N^{-1/3}d_1. \tag{3-1}$$

Both for the water and for the glycerol aqueous solution, the average size of fragmented bubbles was in the range of 50 mm to 200 mm. The size d_2 of fragmented bubbles decreased with a decreasing size d_1 of the initial bubble. For the glycerol aqueous solution, no significant change is observed in the plot, inferring that viscosity does not affect fragmentation in the range of viscosities investigated here. It is interesting that the sizes of fragmented bubbles did not exceed 200 mm in both cases.
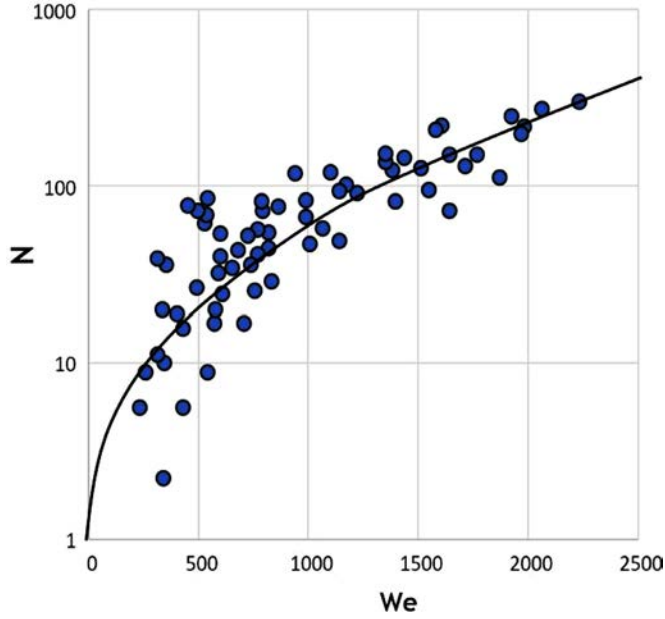
Fig. 6. Fragmentation number versus Weber number defined by Eq. (3-2) in the case of pure water. The curve is fitted adopting Eq. (3-3) and the least-squares approach.
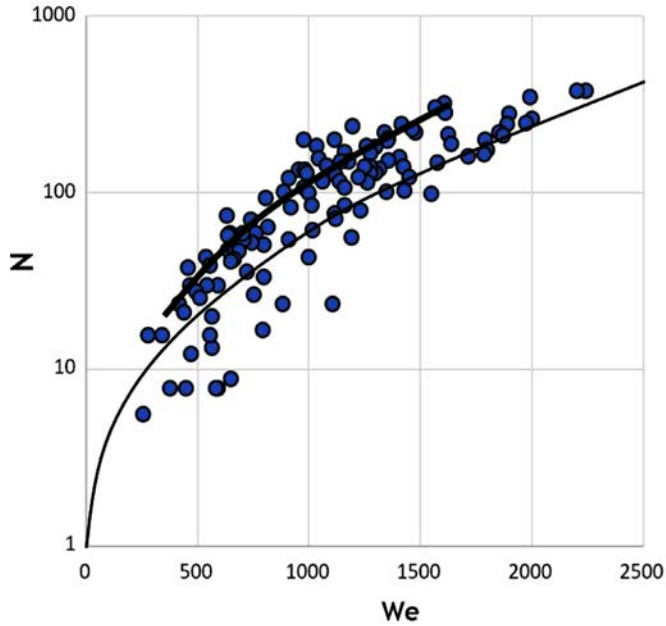

Fig. 7. Fragmentation number versus Weber number defined by Eq. (3-2) in the case of the 30%-glycerol aqueous solution. The thin curve is a function fitted using Eq. (3-3) while the thick curve is a secondary fit drawn manually to highlight a concentrated band in the plot.

Figures 6 and **7** plot the fragmentation number N as a function of the Weber number for pure water and the 30%-glycerol aqueous solution, respectively. The Weber number is defined by

$$We = \frac{\rho u_{th}^2 d_1}{\sigma}, \tag{3-2}$$

where r and σ are respectively the density of the liquid and the surface tension. The fragmentation number increases with the Weber number for both liquids. The maximum fragmentation number was around 350 at $We > 2000$. The thin curve on each graph shows the fitting of a function derived adopting the least-squares

approach, which collapses in both liquids to be

$$N = Int\left[\exp\left(0.22 We^{0.42}\right)\right], \quad 1 \leq We < 2500. \tag{3-3}$$

The exponential function of the powered Weber number infers how effectively bubble fragmentation occurs in the subsonic Venturi tube. From this function, the first emergence of fragmentation (i.e., $N > 1$) is estimated as

$$\exp\left(0.22 We^{0.42}\right) = 2, \quad \rightarrow \quad We = \exp\left[\frac{1}{0.42}\log\left(\frac{\log N}{0.22}\right)\right]$$

$$= 15 = We_c. \tag{3-4}$$

This critical Weber number between $10 < We_c < 20$ corresponds well to data reported in many other studies on bubble fragmentation in various flow geometries. The thick curve in **Fig. 7** indicates a second fitted function that was manually found to pass through a concentrated band in the plot. This curve has a fragmentation number higher than that for Eq. (3-3). This is attributed to the viscous effect which rather promotes bubble fragmentation in a certain range of the Weber number.

3.2. Fragmentation energy efficiency

Theoretically, the energy Δe required to divide a single spherical bubble into N small spherical bubbles is simply expressed as

$$\Delta e = N p_2 V_2 - p_1 V_1 = N \frac{2\sigma}{d_2/2}\left(\frac{1}{6}\pi d_2^3\right) - \frac{2\sigma}{d_1/2}\left(\frac{1}{6}\pi d_1^3\right)$$

$$= \frac{2}{3}\pi\sigma\left(N d_2^2 - d_1^2\right), \tag{3-5}$$

where p is the internal pressure of bubbles due to surface tension σ while V is the volume of a single bubble. As expressed on the far right side of the equation, Δe is a function of the squared bubble diameter, d^2. Because the total mass inside the gas bubble is conserved during fragmentation, Eq. (3–5) can be rewritten for an incompressible state as

$$\Delta e = \frac{2}{3}\pi\sigma d_1^2\left(N^{1/3} - 1\right), \quad \because \frac{1}{6}\pi d_1^3 = N\frac{1}{6}\pi d_2^3. \tag{3-6}$$

The energy required to fragment a single bubble having an initial diameter of d_1 is thus a function of the cubic root of the fragmentation number. This energy is supplied by liquid flow through the bubble's motion relative to the surrounding liquid. To evaluate the energy efficiency, we define

$$\eta = \frac{\Delta e}{E}, \tag{3-7}$$

where E is the energy consumed in driving the single bubble inside the Venturi tube. Thus, η is the ratio of energy conversion to the interfacial energy acquired by the bubble fragmentation. Inside a symmetric Venturi tube (i.e., a tube having the same cross sectional areas for inlet and outlet sections), the consumed energy E is estimated only using the viscous energy dissipation obeying Darcy's law as

$$E = V_1 \cdot \Delta p, \quad \Delta p = \int_0^L \lambda \frac{1}{D(x)} \cdot \frac{1}{2}\rho u_l^2(x) \cdot dx, \tag{3-8}$$

where V_1 is the bubble volume before fragmentation, Δp is pressure loss inside the Venturi tube (energy dissipation per volume), and $u_l(x)$ is the liquid velocity profile as a function of position x. Here, $x=0$ is defined at the center of the throat part (see Fig. 1). $D(x)$ is the local diameter of the Venturi tube and $u(x)$ is the corresponding local liquid velocity. λ is the friction factor of the tube, taking the value around 0.03. The equation of continuity for the liquid phase is

$$Q = \frac{1}{4}\pi D^2(x)u_l(x) = \frac{1}{4}\pi D_{th}^2 u_{th} = const. \tag{3-9}$$
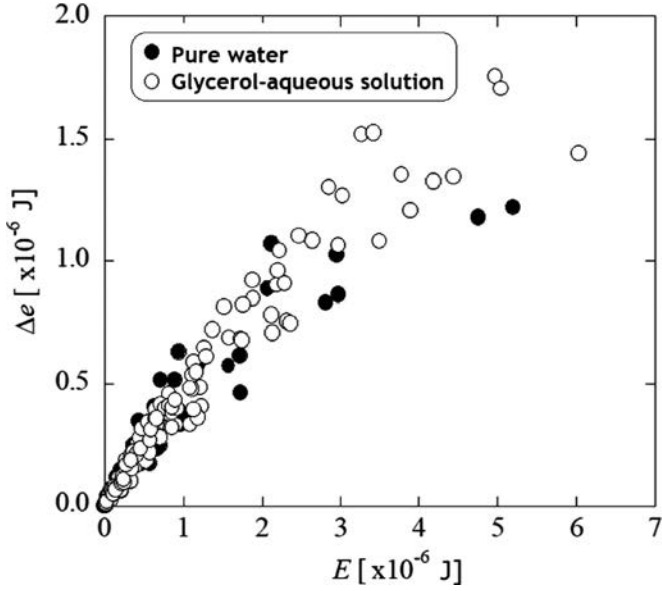
Fig. 8. Relationship between the consumed energy estimated using Eq. (3-10) and the supplied surface energy due to fragmentation measured using Eq. (3-6). A negligible difference in plots between the water and glycerol aqueous solution is confirmed.
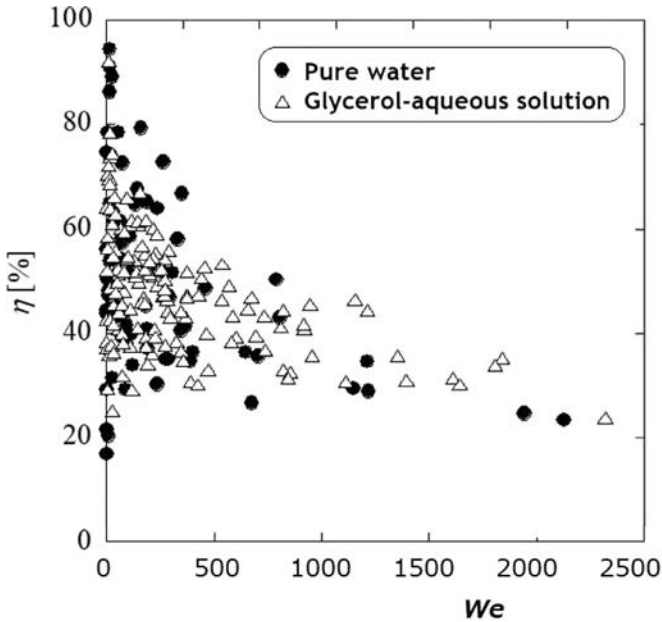

Fig. 9. Bubble fragmentation energy efficiency h defined by Eq. (3-7) having a decreasing trend with an increasing Weber number, showing no significant effect of the viscosity of the liquid. The large deviation in h observed for $We < 100$ originates from the small integer-number dependence of the fragmentation number.

Equation (3-8) is therefore rewritten as

$$E = \frac{8}{\pi^2} \lambda \rho V_1 \cdot Q^2 \int_0^L \frac{1}{D^5(x)} \cdot dx. \tag{3-10}$$

Figure 8 plots the relation between the interfacial energy supply De and consumed energy E for injected bubbles of various size. The general trend is simply an increase in De with E. There is no appreciable difference between the pure water and 30%-glycerol aqueous solution. The corresponding energy efficiency η is plotted as a function of the Weber number in **Fig. 9**. The measured η is of the order of several tens of percent, which means that half the energy consumed in pumping the bubble is used in breaking

up the bubble. Sometimes, η takes a value larger than 80% at the lower limit of the Weber number; i.e., $We \sim We_c = 15$. As the We number increases, h gradually decreases and converges to around $\eta = 20\%$. This dependency on the Weber number is explained by substituting Eqs. (3-6) and (3-10) into Eq. (3-7), yielding

$$\eta = \frac{\pi^2 \sigma}{2\lambda \rho d_1 \cdot Q^2 \int_0^L \frac{1}{D^5(x)} \cdot dx} \left(N^{1/3} - 1 \right). \tag{3-11}$$

Further rewriting with the expression for the Weber number in Eq. (3-2) yields

$$\eta = \frac{8 D_{th}}{\lambda \int_0^L [D_{th}/D(x)]^5 dx} \cdot \frac{N^{1/3} - 1}{We}. \tag{3-12}$$

The energy efficiency thus decreases in inverse proportion to the Weber number. This trend agrees with that of the measurement data. At a low Weber number of $We < 100$, the data of η scatter largely. This is because the regime corresponds to $N < 10$ in Eq. (3-3), in which the integer-number dependence of a single digit sways the efficiency accidentally. However, the average value was around $\eta = 50\%$ in the high Weber number regime.

3.3. Bubble translational motion

How does a bubble acquire interfacial energy in the Venturi tube? The question can be solved by looking at the motion of bubbles. We measured the motion of a bubble and obtained the spatial evolution of the bubble velocity as shown in **Fig. 10(a)**. This is the case of a bubble with $d_1 = 1.0$ mm in water, fragmented at $u_{th} = 11.1$ m/s. The orange curve indicates the liquid flow velocity $u(x)$ in the tube, calculated using the equation of continuity, Eq. (3-9). The bubble had a velocity higher than that of the liquid flow in the converging section at $x < 0$. This was because of the negative pressure gradient of liquid according to Bernoulli's law, which accelerates the bubble forward faster than the liquid flow. Immediately after the throat part, in contrast, the bubble rapidly decelerated to a low velocity and was much slower than the liquid flow there. The deceleration was also due to the pressure gradient that became positive in the diverging part. Therefore, the slip of the bubble from the liquid flow saw sharp switching between converging and diverging parts (**Fig. 10(b)**). The local maximum slip velocity was faster than 5 m/s, which is high for such a small bubble with $d_1 = 1$ mm. This is understood as a major mechanism causing fragmentation.

Figure 11(a) plots the spatial evolution of a bubble's acceleration obtained by differentiating the measured velocity. The magnitude of the acceleration of the bubble was twice that of the liquid. As known from the inviscid theory of a bubble's acceleration (e.g., van Wijngaarden, 1972)

$$\frac{du_b}{dt} = \frac{1+\beta}{\beta} \cdot \frac{du_l}{dt} \approx \frac{1+\beta}{\beta} u_l \frac{du_l}{dx}, \tag{3-13}$$

twice the liquid acceleration means the added mass coefficient of the bubble is $\beta = 1$, which is greater than that of a spherical bubble at $\beta = 1/2$. This is attributed to the bubble's expansion in the radial direction of the Venturi tube. Instantaneously, the acceleration is of the order of 50,000 m/s^2; i.e., 5000 times the acceleration due to gravity. Moreover, the bubble acceleration has two negative peaks, which are near the inlet and outlet of the throat part. This infers a shaking action of bubbles in the streamwise direction that activates the shape deformation.

Figure 11(b) shows the spatial evolution of force components acting on the bubbles in the streamwise direction. In this computation, the added inertia force F_A (Michaelides, 1997) is obtained
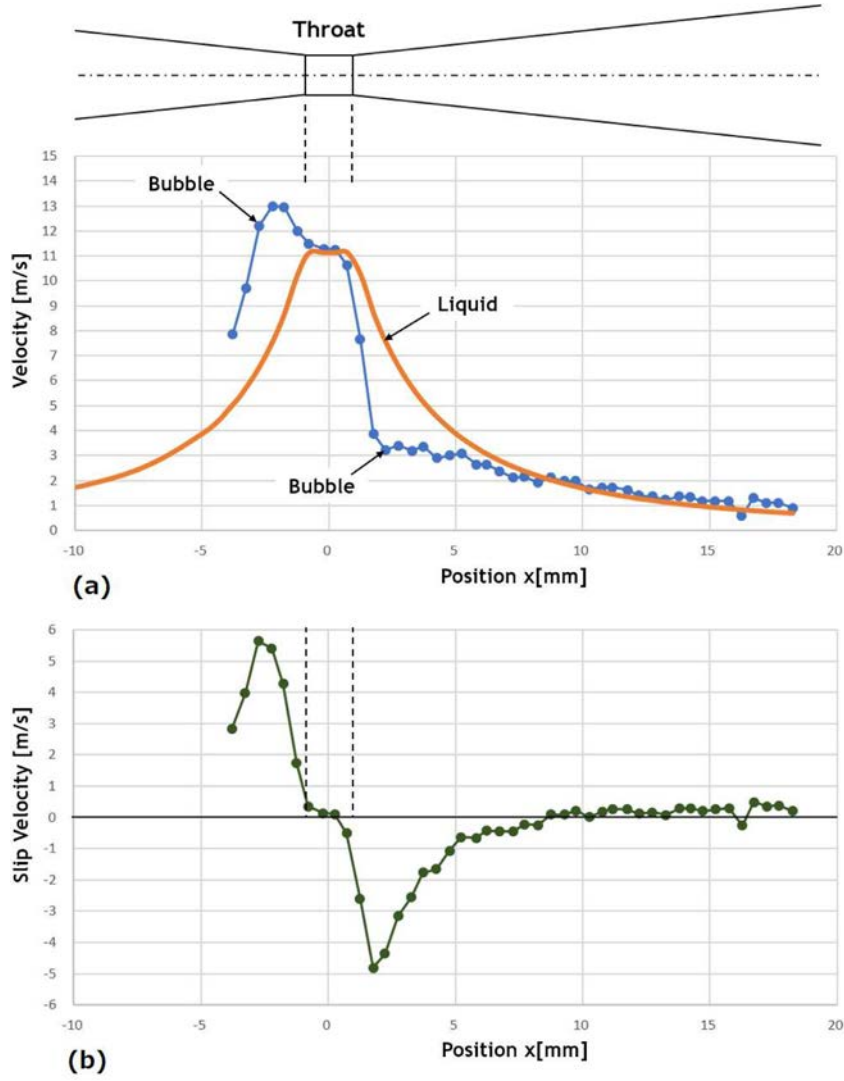
Fig. 10. Kinematics of bubbles measured by bubble tracking in consecutive images for $u_{th} = 11.1$ m/s and $d_1 = 1.0$ mm: (a) spatial evolution of the bubble velocity (blue dots) and liquid flow velocity (orange curve) estimated using Eq. (3-9) and (b) slip velocity of the bubble from the liquid flow velocity displaying a sharp reversal.

from the measured velocity as

$$F_A = \beta \rho V \left[\frac{du_b(x)}{dt} - \frac{Du_l(x)}{Dt} \right] = \beta \rho V \left[\frac{du_b(x)}{dt} - u_l(x) \frac{du_l(x)}{dx} \right]. \tag{3-14}$$

The pressure gradient force F_P is obtained via Bernoulli's law as

$$F_P = V \frac{dp(x)}{dx}, \quad p(x) = p_0 - \frac{1}{2}\rho u_l^2(x). \tag{3-15}$$

Thus,

$$F_P = -\rho V \cdot u_l(x) \frac{du_l(x)}{dx}. \tag{3-16}$$

The drag force F_D is estimated using the force balance equation as

$$F_A + F_P + F_D = 0, \quad F_D = -(F_A + F_P). \tag{3-17}$$

The magnitudes of the three force components are of the same order, approximately 1 mN. The pressure gradient force and drag force strongly oscillated as a pair of positive and negative pulses, mostly in directions opposite to each other. During these oscillations, the added inertia force fluctuated in two cycles of the pair.

Considering these fluctuations of forces accompanying changes in signs, the excitation of bubble deformation and resultant fragmentation are explained next.

4. Theoretical interpretation of fragmentation

In this section, we explain experimental results based on the fundamental theory of bubble dynamics. All possible governing factors are considered in seeking the dominant factor promoting bubble fragmentation.

4.1. Pressure gradient profile

From Bernoulli's theorem, the pressure profile inside the Venturi tube based on the inviscid assumption is estimated as

$$p(x) = p_0 - \frac{1}{2}\rho u_l^2(x), \tag{4-1}$$

where p_0 is the ambient pressure outside the Venturi tube. The liquid velocity is given by the tube diameter profile $D(x)$ obtained from the equation of continuity as

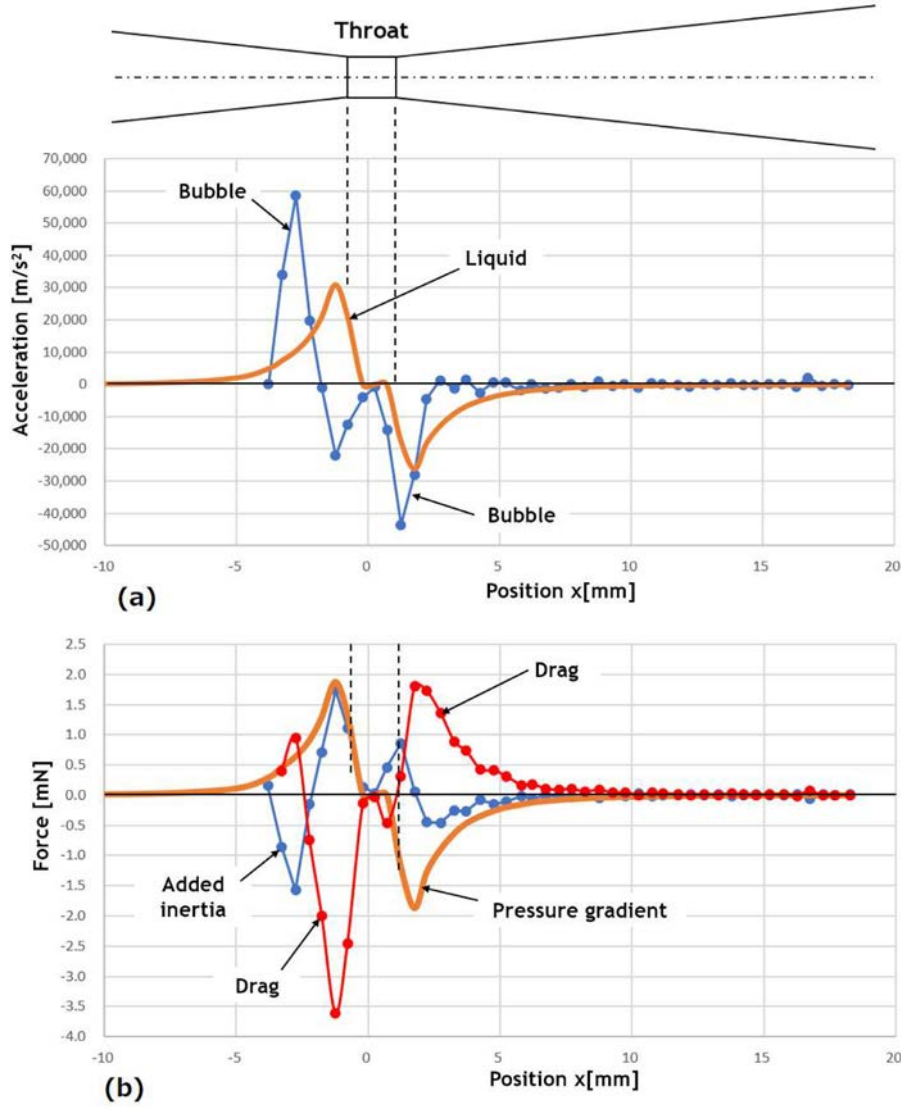$$u_l(x) = Q\left[\frac{1}{4}\pi D^2(x)\right]^{-1}. \tag{4-2}$$

Fig. 11. Dynamics of a bubble obtained from the measured bubble velocity evolution for $u_{th} = 11.1$ m/s and $d_l = 1.0$ mm: (a) spatial evolution of the bubble's Lagrangian acceleration compared with the convective acceleration of liquid flow and (b) the bubble's force components obtained from the acceleration using Eqs. (3-14), (3-16), and (3-17).

The pressure gradient profile is therefore

$$\frac{dp}{dx}(x) = -\rho u_l(x)\frac{du_l(x)}{dx} = \frac{32\rho Q^2}{\pi^2 D^5(x)} \cdot \frac{dD(x)}{dx}. \tag{4-3}$$

Equation (4-3) tells us that the local pressure gradient, which drives bubble motion in the liquid, is sharply magnified when using a small diameter of the Venturi tube (according to the negative fifth power of the diameter).

4.2. Translational velocity profile of a bubble

The bubble velocity u_b is the sum of the liquid velocity u_l plus the slip velocity relative to the liquid u_s:

$$u_b(x) = u_l(x) + u_s(x), \quad u_l(x) = \frac{Q}{A(x)}, \tag{4-4}$$

where $A(x)$ is the cross-sectional area of the tube at position x. In the case of spherical bubbles, the terminal slip velocity (without acceleration) is estimated using the force balance between the local pressure gradient and drag force,

$$V\frac{dp(x)}{dx} = -C_d\frac{1}{2}\rho|u_s(x)|u_s(x) \cdot \frac{1}{4}\pi d^2, \quad V = \frac{1}{6}\pi d^3, \tag{4-5}$$

where C_d is the drag coefficient of the bubble, which is modeled using either the following Reynolds number or Weber number, defined by the slip velocity, u_s (Magnaudet and Eames, 2000):

$$Re_s = \frac{|u_s|d}{\nu}, \quad We_s = \frac{\rho|u_s|^2 d}{\sigma}. \tag{4-6}$$

According to measurement data of the slip velocity, Re_s and We_s are respectively within the ranges of $500 < Re_s < 5000$ and $10 < We_s < 2500$. This means that drag departs from the Reynolds number dependence regime and can be approximated by a constant value around $C_d \sim 1$ (Bhaga and Weber, 1981). The combination of Eqs. (4-3) and (4-5) leads to

$$|u_s(x)|u_s(x) = -\frac{4d}{3C_d\rho}\cdot\frac{dp(x)}{dx} = -\frac{128}{3C_d}\cdot\frac{Q^2 d}{\pi^2 D^5(x)}\cdot\frac{dD(x)}{dx}. \tag{4-7}$$

The sign of the slip velocity depends on the sign of dD/dx; i.e., the position of the bubble. The slip velocity is thus given by

$$\begin{aligned} u_s(x) = +\frac{8Q}{\pi D^2(x)}\sqrt{\frac{2}{3C_d}\cdot\frac{d}{D(x)}\cdot\left|\frac{dD(x)}{dx}\right|} \quad for \ \frac{dD(x)}{dx} \le 0, \\ u_s(x) = -\frac{8Q}{\pi D^2(x)}\sqrt{\frac{2}{3C_d}\cdot\frac{d}{D(x)}\cdot\left|\frac{dD(x)}{dx}\right|} \quad for \ \frac{dD(x)}{dx} > 0. \end{aligned} \tag{4-8}$$
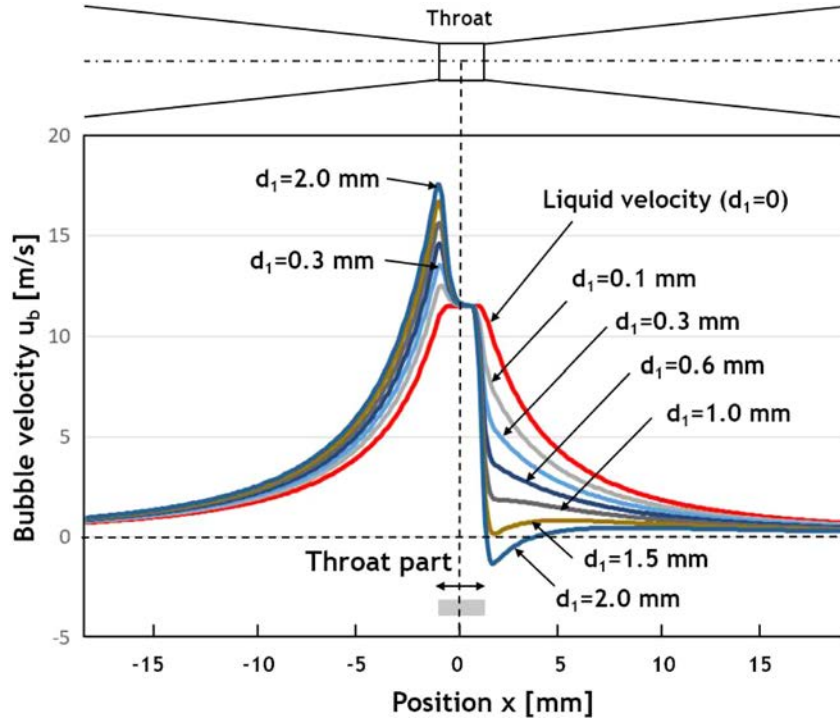
Fig. 12. Theoretical bubble velocity profile inside the symmetric Venturi tube at u_{th} = 11.5 m/s (Q = 2.10 l/min) obtained using Eq. (4-9) for various sizes of bubble, confirming similarity with the measured bubble velocity shown in Fig. 10 (a).

Using Eq. (4-4), the bubble's absolute velocity is derived as

$$u_b(x) = \frac{4Q}{\pi D^2(x)}\left[1 \pm 2\sqrt{\frac{2}{3C_d} \cdot \frac{d}{D(x)} \cdot \left|\frac{dD(x)}{dx}\right|}\,\right],\qquad(4\text{-}9)$$

where the plus and minus signs in Eq. (4-9) correspond to the converging and diverging parts of the Venturi tube, respectively.

Using the geometric parameters of the present Venturi tube, Eq. (4-9) is calculated to obtain the bubble velocity profile shown in **Fig. 12**. A red curve indicates the liquid velocity profile. The bubble travels faster than the liquid flow in the converging part at $dD(x)/dx < 0$ and accelerates until entering the throat part because of a gradual decrease in $D(x)$. In contrast, the bubble passing through the throat part sharply slows down and experiences a large negative slip from the liquid flow; i.e., the bubble slips back and resists transportation by the liquid flow. The estimation data for d_1 = 1.0 mm agree well with the measurement data in **Fig. 10(a)**. The trend is more remarkable for a larger bubble. The bubble with a diameter of $d_1 > 1.5$ mm has zero or negative velocity in the diverging part. This means that such a bubble will be trapped there and does not pass through the tube. Soubiran and Sherwood (2000) theoretically estimated a possibility of bubble's oscillation within the region of negative velocity if bubbles keep their size. In reality, the bubble in this region are fragmented and conveyed downstream obeying the different curves of smaller diameter in the diagram. This two-phase flow dynamics allow the Venturi tube to act like a high-pass filter for the bubble size. This function is regarded an important mechanism for converting large bubbles to microbubbles.

4.3. Bubble slip characteristics

The maximum slip-back velocity of a bubble in the diverging part is calculated using Eq. (4-8) as depicted in **Fig. 13**. The slip-back velocity increases with the throat flow velocity u_{th}. The trend is amplified by enlarging the initial bubble size d_1. This explains

why a large bubble can be fragmented easily. **Figure 14** presents the slip storage distance, which is defined by

$$S_x = \int_0^\infty [u_l(x) - u_b(x)] \cdot dt = \int_0^L \left[\frac{u_l(x)}{u_b(x)} - 1\right] \cdot dx,$$

$$\because dx = u_b(x) \cdot dt. \qquad(4\text{-}10)$$

The distance refers to the delay in the bubble outflow relative to the liquid flow with a unit of distance. The distance S_x increases with the throat flow velocity u_{th} and the bubble diameter d_1. For a small bubble having a diameter of $d_1 < 0.2$ mm, the distance is shorter than the length of the diverging part; i.e., $S_x < L$. In contrast, a large bubble corresponds to a distance longer than L as the throat flow velocity increases.

Figure 15 depicts the bubble's relative residual time R_t, which is defined by

$$R_t = \frac{T_b}{T_l} = \int_0^L \frac{1}{u_b(x)}dx / \int_0^L \frac{1}{u_l(x)}dx,\qquad(4\text{-}11)$$

where T_b is the residual time that the bubble remains within the diverging part at $x < L$ while T_l is that for liquid. The data show that a large bubble has a large ratio, implying that such a bubble comes to the outlet of the Venturi tube late in comparison with the liquid flow. At $d_1 > 2$ mm, the bubble velocity is zero such that there is local bubble trapping, and the residual time increases to infinity. Thus, the large bubble, which maintains its size, does not exit the Venturi tube.

The critical bubble diameter for falling in the trapping condition, d_c, is theoretically derived from Eq. (4-9) by setting $u_b = 0$ as

$$\frac{8}{3C_d} \cdot \frac{d}{D(x)} \cdot \frac{dD(x)}{dx} = 1, \;\rightarrow\; d = d_c \equiv \frac{3C_d}{8} \cdot D(x)\left(\frac{dD(x)}{dx}\right)^{-1}.$$

$$(4\text{-}12)$$

This equation shows that the diameter of the trapped bubble is independent of the flow speed u_{th} and flow rate Q, as long as C_d
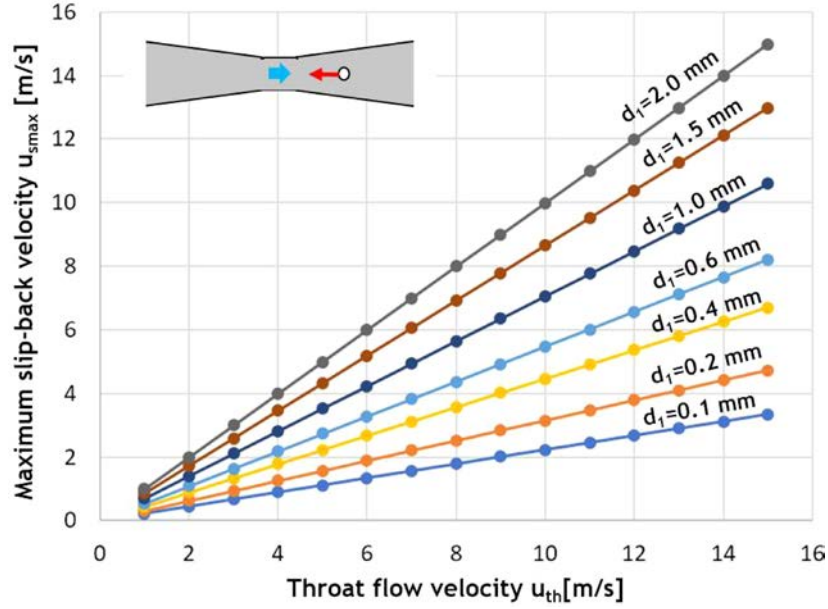
Fig. 13. Maximum slip-back velocity of bubbles in the diverging part as the throat flow velocity increases, calculated using Eq. (4-8) for $dD/dx > 0$. Greater slip-back velocities occur for larger injected bubbles.
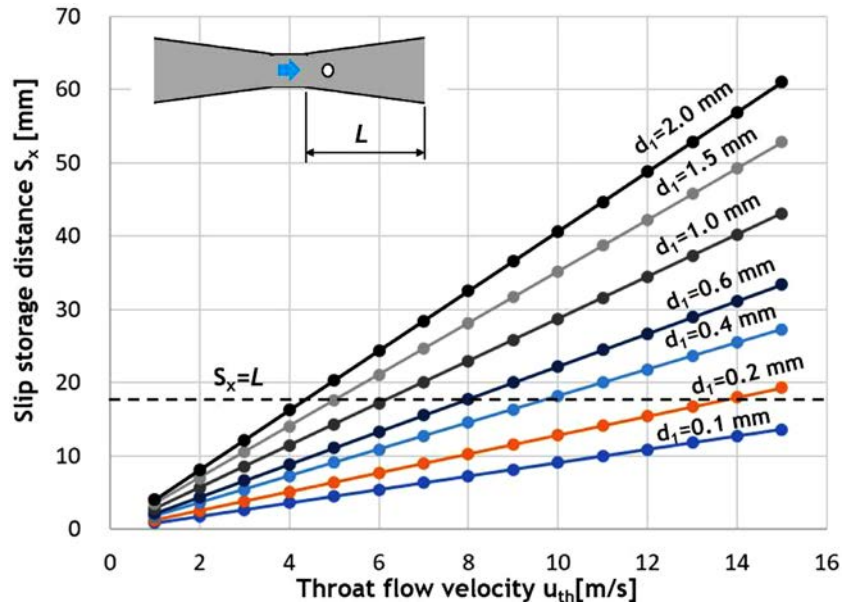

Fig. 14. Slip storage distance of bubbles calculated with Eq. (4-10) for various sizes of bubble. Large bubbles have a longer slip storage as the throat flow velocity increases.

is unmodified. The diameter is determined by the geometric profile, $D(x)$. The local tube diameter at which bubbles are trapped is estimated from Eq. (4-12) as

$$D(x) = \frac{8}{3C_d} \cdot \frac{dD(x)}{dx} d. \tag{4-13}$$

The present Venturi tube has the diameter profile of

$$D(x) = D_{th} + \frac{x - x_0}{L}(D_o - D_{th}), \ x_0 \le x \le L, \tag{4-14}$$

where $x_0 = 1$ mm as the rear edge position of the throat part, D_o is the outlet diameter and L is the streamwise length of the diverging part. Substituting this equation into Eq. (4-13) gives the trapping position x_t as

$$x = x_t = x_0 + \frac{L}{D_0/D_{th} - 1}\left[\frac{8}{3C_d} \cdot \frac{d}{L}\left(\frac{D_o}{D_{th}} - 1\right) - 1\right]. \tag{4-15}$$

This equation shows that a larger bubble is trapped at a more downstream position. If the position is outside the diverging part (i.e., $x_t > L$), the tube does not work as a bubble size filter. To satisfy $x_t < L$, we require the initial bubble size to meet the condition that

$$\frac{d}{L} < \frac{3C_d}{8}\left(1 - \frac{x_0}{L} + \frac{D_{th}/D_o}{1 - D_{th}/D_o}\right), \tag{4-16}$$

where the term in the parenthesis is approximately unity, therefore,

$$d < \frac{3C_d}{8}L. \tag{4-17}$$

Namely, the initial bubble diameter should be small enough to realize bubble trapping inside the diverging part. In the regime of a spherical cap bubble, $C_d \sim 1/4$ thus $d < 0.1L$ should be satisfied.
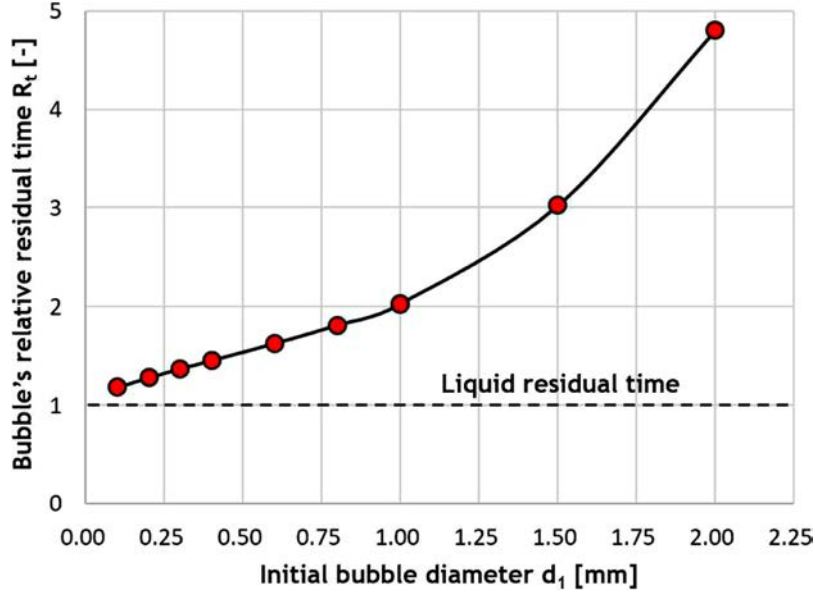
Fig. 15. A bubble's residual time inside the diverging part of the tube relative to the liquid residual time, calculated with Eq. (4-11), demonstrating long-term interaction between the two phases as the initial bubble diameter d_1 increases.

We next evaluate the supply of energy from the liquid to a single bubble as the bubble slowly migrates in the diverging part. The energy is estimated from

$$de = F \cdot [u_l(x) - u_b(x)]dt = F \cdot [u_l(x) - u_b(x)]\frac{1}{u_b(x)}dx, \quad (4\text{-}18)$$

where F is the force acting on the bubble due to the pressure gradient,

$$F = V\frac{dp}{dx}(x) = -\rho V \cdot u_l(x)\frac{du_l(x)}{dx}. \quad (4\text{-}19)$$

Therefore, the total energy transferred to the bubble in the diverging part at $0 < x < L$ is

$$\begin{aligned}
E_b &= \int_0^L F \cdot [u_l(x) - u_b(x)]\frac{1}{u_b(x)}dx \\
&= \frac{1}{6}\pi d^3 \rho \int_0^L u_l(x)\frac{du_l(x)}{dx}\left[1 - \frac{u_l(x)}{u_b(x)}\right] \cdot dx.
\end{aligned} \quad (4\text{-}20)$$

Using Eq. (4-4) and Eq. (4-9), the numerical solution for Eq. (4-20) is obtained as shown in **Fig. 16**. The results indicate that the energy increases exponentially with the bubble diameter (where the ordinate is a logarithmic scale). The energy also increases with the throat flow velocity u_{th}. A large bubble thus receives much energy during its advection, which promotes fragmentation. A comparison with the measurement data in **Fig. 8** reveals that the energy acquired by fragmentation is of the order of a few microjoules for a single bubble with $d_1 = 1.0$ mm. This energy level matches the present estimation.

4.4. Fragmentation triggered by oscillation of a bubble's shape

Natural frequency of shape oscillation of a bubble with a diameter d_1 in quiescent liquid is described by

$$f_n = \frac{1}{2\pi}\sqrt{(n-1)(n+1)(n+2)\frac{8\sigma}{\rho d_1^3}}, \quad \rightarrow \quad f_2 = \frac{2}{\pi}\sqrt{\frac{6\sigma}{\rho d_1^3}}, \quad (4\text{-}21)$$

where n is the mode of shape oscillation; i.e., $n = 2$ refers to ellipsoidal deformation and $n = 3$ refers to triangular deformation (Feng and Leal, 1977). In the diverging part of the Venturi tube, the liquid flow experiences Lagrangian pressure fluctuation of a half wavelength at $0 < x < L$. The liquid pressure p thus fluctuates at a characteristic frequency of

$$f_l \approx \frac{1}{2L} \cdot \frac{1}{L}\int_0^L u_l(x)dx \approx \frac{5}{64} \cdot \frac{u_{th}}{L}, \quad (4\text{-}22)$$

where Eq. (4-2) and Eq. (4-14) are applied to the spatial integration of liquid velocity. The acceleration of the bubble depends on the added mass coefficient β, and the bubble experiences fluctuation of the liquid pressure at a frequency of

$$f_b = \left(1 + \frac{1}{\beta}\right)f_l = \frac{5}{64}\left(1 + \frac{1}{\beta}\right) \cdot \frac{u_{th}}{L}. \quad (4\text{-}23)$$

The matching condition $f_b = f_n$ in the lowest mode of shape oscillation (i.e., ellipsoidal mode at $n = 2$) is described by

$$\frac{5}{64}\left(1 + \frac{1}{\beta}\right) \cdot \frac{u_{th}}{L} = \frac{1}{\pi}\sqrt{\frac{6\sigma}{\rho d_1^3}} \rightarrow u_{th} = \left(1 + \frac{1}{\beta}\right)^{-1}\frac{64L}{5\pi}\sqrt{\frac{6\sigma}{\rho d_1^3}}. \quad (4\text{-}24)$$

For the present configuration of the Venturi tube, the throat flow speed at this resonance is calculated as $u_{th} = 3.6$ m/s for $d_1 = 1$ mm and $u_{th} = 10.1$ m/s for $d_1 = 0.5$ mm. These speeds are easily realized and overlap with the present experimental conditions for subsonic bubble fragmentation. The flow speed in Eq. (4-24) is rewritten using the Weber number as

$$We \cdot \left(\frac{d_1}{L}\right)^2 = 6\left(1 + \frac{1}{\beta}\right)^{-2}\left(\frac{64}{5\pi}\right)^2 \cong 11. \quad (4\text{-}25)$$

As an example, the combination of a bubble size of $d_1/L = 0.1$ and $We = 1100$ excites ellipsoidal deformation. Such matching occurs for a single value of the Weber number for a given bubble size. This explains why scattering was observed for the fragmentation number and energy efficiency **Fig. 9**). It is worth noting that the shape oscillation mode of $n > 2$ has a high frequency (Eq. (4-21)), and the matching flow speed departs the subsonic condition of bubbly flow, being faster than the speed of sound. That is to say, the initial trigger of bubble fragmentation in the subsonic Venturi tube relies on ellipsoidal shape oscillation.
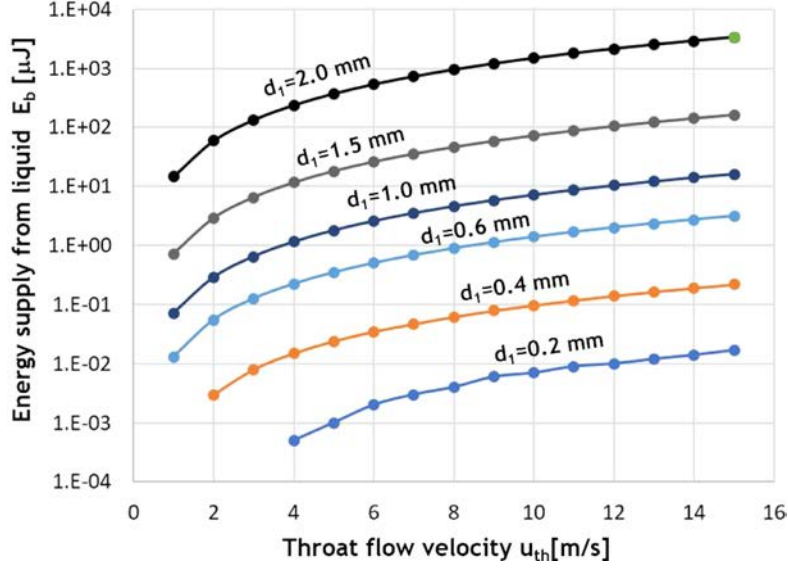
Fig. 16. Supply of energy from the liquid to a single bubble estimated using Eq. (4-20). The energy increases with the throat flow velocity u_{th} and the initial bubble diameter d_1.

4.5. Effect of the bubble's volumetric motion

Even in nearly incompressible flow at $Ma < 0.3$, bubbles have a resonance frequency in terms of volume oscillation, which might trigger fragmentation. The Rayleigh–Plesset equation is

$$\rho\left\{r_b\frac{d^2r_b}{dt^2} + \frac{3}{2}\left(\frac{dr_b}{dt}\right)^2\right\} = p_b - \frac{2\sigma}{r_b} - \frac{4\mu}{r_b}\left(\frac{dr_b}{dt}\right)$$
$$- \left\{p - \frac{1}{4}\rho|u_b - u_l|^2\right\}, \qquad (4\text{-}26)$$

where r_b is the bubble radius; i.e., $r_b = d_1/2$. p_b is the gas pressure inside the bubble. For a small fluctuation in bubble size around the diameter d_1, the resonance frequency of volumetric oscillation (Plesset and Prosperetti, 1977) is derived as

$$f_v = \frac{1}{\pi d_1}\sqrt{\frac{1}{\rho}\left(3p + \frac{8\sigma}{d_1}\right)}. \qquad (4\text{-}27)$$

The frequency takes the value $f_v = 3$ kHz in the case of a bubble with $d_1 = 1$ mm at atmospheric pressure, $p = 10^5$ Pa. Inside the Venturi tube, the liquid pressure has a streamwise profile (Eq. (4-1)), and it takes its lowest value in the throat part as

$$p_{th} = p_0 - \frac{1}{2}\rho u_{th}^2. \qquad (4\text{-}28)$$

Substituting p_{th} into p in Eq. (4-27) gives

$$f_v = \frac{1}{\pi d_1}\sqrt{\frac{1}{\rho}\left[3\left(p_0 - \frac{1}{2}\rho u_{th}^2\right) + \frac{8\sigma}{d_1}\right]}. \qquad (4\text{-}29)$$

The matching condition of this frequency f_v with the pressure fluctuation frequency f_b (Eq. (4-23)) is described by

$$\frac{5}{64}\left(1 + \frac{1}{\beta}\right)\cdot\frac{u_{th}}{L} = \frac{1}{\pi d_1}\sqrt{\frac{1}{\rho}\left[3\left(p_0 - \frac{1}{2}\rho u_{th}^2\right) + \frac{8\sigma}{d_1}\right]}. \qquad (4\text{-}30)$$

The solution to the equation for the throat flow velocity is obtained as

$$u_{th} = \sqrt{\frac{\frac{2}{\rho}\left(p_0 + \frac{8\sigma}{3d_1}\right)}{1 + \frac{2}{3}\left[\frac{5}{64}\left(1 + \frac{1}{\beta}\right)\right]^2\left(\frac{\pi d_1}{L}\right)^2}}. \qquad (4\text{-}31)$$

In operation with the atmospheric pressure ambience, i.e., $p_0 \gg \sigma/d_1$ and $d/L \ll 1$, Eq. (4-31) is approximated as

$$u_{th} = \sqrt{\frac{2p_0}{\rho}}, \qquad (4\text{-}32)$$

and u_{th} becomes independent of the bubble size, d_1, in terms of the resonance condition. This is because the bubble size dependency is cancelled out by pressure lowering inside the throat part. Equation (4-32) estimates the throat flow velocity at $u_{th} = 14$ m/s for any case as the ambient pressure is $p_0 = 10^5$. This value is higher than the present maximum flow speed, and the effect of the volumetric oscillation is thus regarded as a negligible factor in subsonic bubble fragmentation.

4.6. Effect of velocity gradient in liquid phase

The velocity gradient tensor field of liquid phase inside the Venturi tube also influences on bubble fragmentation (Sherwood, 2000). Two-dimensional components are generally described as

$$[D] = \begin{bmatrix} \frac{\partial u}{\partial x} & \frac{\partial u}{\partial y} \\ \frac{\partial v}{\partial x} & \frac{\partial v}{\partial y} \end{bmatrix} = \frac{1}{2}\begin{bmatrix} 2\varepsilon_x & \gamma_{xy} \\ \gamma_{xy} & 2\varepsilon_y \end{bmatrix} + \frac{1}{2}\begin{bmatrix} 0 & -\omega_z \\ \omega_z & 0 \end{bmatrix}, \qquad (4\text{-}33)$$

where ε, γ, and ω are stretch, shear, and rotation rates. Inside the diverging part of the Venturi tube, magnitude of the stretching rate is estimated as

$$\varepsilon = \sqrt{\varepsilon_x^2 + \varepsilon_y^2} \approx \sqrt{2\frac{U_o}{L}\left[1 - \left(\frac{D_{th}}{D_o}\right)^2\right]} \approx \sqrt{\frac{2U_o}{L}}, \qquad (4\text{-}34)$$

where subscript o stands for the inlet plane of the tube. Magnitudes of shear rate and rotation rate are scaled as

$$\gamma = \sqrt{2\gamma_{xr}^2} \approx \sqrt{\frac{U_o + U_{th}}{D_o + D_{th}}} \approx \sqrt{\frac{U_{th}}{D_o}}, \qquad (4\text{-}35)$$

$$\omega = \sqrt{2\omega_z^2} \approx \sqrt{\frac{U_{th}}{D_o}}. \qquad (4\text{-}36)$$

Substituting our experimental conditions into these three formulae provides $\epsilon = 40$ s^{-1} and $\gamma = \omega = 200$ s^{-1}. In contrast, bubble's slip back due to high positive pressure gradient takes the bubble's relative velocity to the liquid phase over 5 m/s as shown in
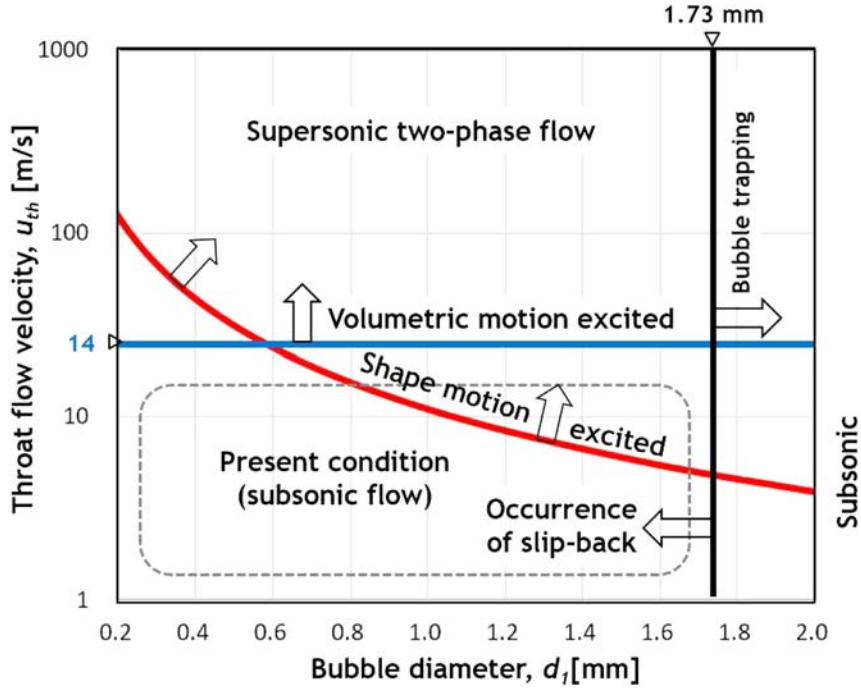
Fig. 17. Throat flow velocities for three types of bubble motion in the present Venturi tube. The vertical black line is the criterion of a bubble's slip-back estimated using Eq. (4-41), the red curve shows resonance with ellipsoidal shape motion given by Eq. (4-42), and the horizontal blue line is the border of excitation in volumetric motion estimated using Eq. (4-32).

Fig. 10. This effect can be represented by bubble stretching rate which is given by streamwise velocity gradient in terms of bubble's relative velocity to liquid phase as

$$\varepsilon_b = \left| \frac{\Delta(u_b - u_l)}{\Delta x} \right|. \qquad (4\text{-}37)$$

The value of ϵ_b is approximated to be $6/0.002 = 3000$ s^{-1}, which is much greater than ϵ, γ, and ω of liquid phase. Therefore, we can conclude that bubble's fragmentation in the Venturi tube is dominated by bubble's rapid translational motion driven by pressure gradient. Contribution of shear in the base flow is not a primary factor to govern the microbubble generation.

4.7. Fragmentation associated to energy dissipation rate

Martinez-Bazan et al. (2010) reported a scaling for the limit of bubble fragmentation caused by turbulence in the liquid phase. They indicated a critical Weber number which is a function of turbulent dissipation rate ϵ_t as

$$We_t = \frac{\rho \varepsilon_t^{2/3} d^{5/3}}{\sigma}, \qquad (4\text{-}38)$$

where d stands for bubble diameter survival in turbulence. In the present Venturi tube, bubble fragmentation occurred without significant help of stress field of liquid phase. Hence, the phenomenon is scaled by the following Weber number defined by the slip velocity,

$$We_s = \frac{\rho(u_b - u_l)^2 d}{\sigma}, \qquad (4\text{-}39)$$

where u_b and u_l are for the velocity of bubble and liquid phases, respectively. If Eq. (4-38) can stand extensively to estimate the bubble fragmentation limit, $We_t = We_s$ can be assumed to obtain

$$\frac{\rho \varepsilon_t^{2/3} d^{5/3}}{\sigma} = \frac{\rho(u_b - u_l)^2 d}{\sigma}, \; \rightarrow \; \varepsilon_t = \frac{(u_b - u_l)^3}{d}. \qquad (4\text{-}40)$$

Now ϵ_t corresponds to energy dissipation rate of bubble, which is proportional to the relative velocity cubed. According to the present measured data, the order of ϵ_t is estimated to be 5^3 $(100 \times 10^{-6})^{-1} \sim 10^6$ m^2/s^3. Substituting this value to Eq. (4-38) leads to $We_t = We_s = 30$. The value is of the same order of We_c defined in Eq. (3-4).

4.8. Summary of bubble fragmentation

To find the trigger of bubble fragmentation in the Venturi tube, three types of bubble dynamics were discussed above: (1) the bubble's rapid slip-back in translational motion, (2) the bubble's shape oscillation, and (3) the bubble's volumetric oscillation. The critical condition for exciting these bubble motions was derived as a mutual relation between the throat flow velocity and the bubble diameter as below.

1) Translational motion (slip-back condition):

$$d_1 < \frac{3C_d}{8\pi} L \approx 0.1 \times L. \qquad (4\text{-}41)$$

2) Shape motion (ellipsoidal shape oscillation condition):

$$u_{th} = \left(1 + \frac{1}{\beta} \right)^{-1} \frac{64L}{5\pi} \sqrt{\frac{6\sigma}{\rho d_1{}^3}} \propto d_1^{-3/2}. \qquad (4\text{-}42)$$

3) Volumetric motion:

$$u_{th} = \sqrt{\frac{2p_0}{\rho}} \propto d_1{}^0 = const.. \qquad (4\text{-}43)$$

Figure 17 presents the relationship between the above three types of throat flow velocity and the initial bubble diameter. Equation (4-41) gives $d < 1.73$ mm for the present geometry of the Venturi tube, which is indicated by a black vertical line. On the left side of the line, there is bubble slip-back regardless of the throat flow velocity. A bubble in this case receives much energy from liquid flow for a long period in the diverging part. Only the fragmented bubbles migrate downstream, such that the Venturi tube

works as a bubble size filter. In the present subsonic experimental range at $u_{th} < 12$ m/s, the excitation of shape motion estimated using Eq. (4-42) overlaps as indicated by the red curve in the diagram. This enhances rapid bubble distortion and bubble fragmentation for bubbles larger than 0.8 mm so that the fragmentation number exceeds 100 at $We > 1500$ (see **Figs. 6** and **7**). However, it matches the resonance frequency in a discrete manner so that scattering of the resultant bubble fragmentation number becomes remarkable. In contrast, the excitation of volumetric oscillation begins at a throat flow velocity of $u_{th} > 14$ m/s. This factor is concluded to be irrelevant to bubble fragmentation in subsonic operation.

5. Conclusions

Bubble fragmentation in a Venturi-type microbubble generator was investigated experimentally and theoretically. We focused on the performance and mechanism of bubble fragmentation realized under subsonic flow conditions; i.e., we investigated how a single bubble breaks down to microbubbles without a pressure shock wave. The number of microbubbles ranged from 20 to 400, depending on the initial bubble size. This relation collapsed to a single formula as a function of the Weber number; i.e., an exponential function of the powered Weber number (Eq. (3-3)). The energy efficiency of fragmentation ranged from 30 to 50 percent. Bubble tracking measurements made from high-speed images revealed rapid bubble deceleration in the diverging part of the tube. This motion resulted in a high slip-back velocity relative to the liquid flow; i.e., a slip velocity exceeding 5 m/s even for bubbles smaller than 1 mm in water. During the deceleration, the three force components of the bubble (i.e., the drag, pressure gradient force, and added inertia force) had fluctuation amplitudes of the same order. Theoretical analysis supported these measurement results and led to the conclusion that slip-back promoted fragmentation most dominantly. It also explained that a bubble larger than the critical size given by Eq. (4-41) cannot migrate downstream before fragmentation. Such dynamics of the bubbles mean that the subsonic Venturi tube primarily functions as a microbubble generator. Furthermore, resonance with natural shape oscillation of a bubble raised the fragmentation number to $N > 100$ at $We > 1000$, but with a scattering due to resonance occurring in a discrete manner.

Declaration of Competing Interest

The authors whose name are listed below certify that they have NO affiliations with or involvement in any organization or entity with any financial interest (such as honoraria; educational grants; participation in speakers' bureaus; membership, employment, consultancies, stock ownership, or other equity interest; and expert testimony or patent-licensing arrangements), or non-financial interest (such as personal or professional relationships, affiliations, knowledge of beliefs) in the subject matter or materials discussed in this manuscript.

CRediT authorship contribution statement

Yuichi Murai: Conceptualization, Methodology, Writing – original draft. **Yuji Tasaka:** Writing – original draft, Writing – review & editing. **Yoshihiko Oishi:** Visualization, Writing – review & editing. **Patricia Ern:** Writing – review & editing.

Acknowledgment

References

Agarwal, A., Jern Ng, W., Liu, Y., 2011. Principle and applications of microbubble and nanobubble technology for water treatment. Chemosphere 84, 1175–1180.

Bhaga, D., Weber, M.E., 1981. Bubbles in viscous liquids: shapes, wakes and velocities. Journal of Fluid Mechanics 105, 61–85.

Calgaroto, S., Wilberg, K, Q., Rubio, J., 2014. On the nanobubbles interfacial properties and future applications in floatation. Mineral Engineering 60, 33–40.

Cheng, W., Murai, Y., Sasaki, T., Yamamoto, F., 2005. Bubble velocity measurement with recursive cross correlation PIV technique. Flow Measurement and Instrumentation 16, 35–46.

Feng, Z.C., Leal, L.G., 1997. Nonlinear bubble dynamics. Annual Rev. Fluid Mechanics 29, 201–243.

Hara, K, Suzuki, T., Yamamoto, F., 2011. Image analysis applied to study on frictional-drag reduction by electrolytic microbubbles in a turbulent channel flow. Exp. Fluids 50, 715–727.

Huang, J., Sun, L, Mo, Z., Liu, H., Du, M., Tang, J., Bao, J., 2019. A visualized study of bubble breakup in small rectangular Venturi channels. Experimental and Computational Multiphase Flow 1, 177–185.

Huang, J., Sun, L., Du, M., Liang, Z., Mo, Z, Tang, J., Xie, G., 2020. An investigation on the performance of a micro-scale Venturi bubble generator. Chemical Engineering Journal 386, 120980.

Kuroshima, R., Otaka, T., Kado, H., 2014. The mechanism of micro-bubble generation in a two dimensional Venturi tube. Transaction of the JSME 80 (2014) fe0318 (in Japanese).

Ichikawa, K., Maeda, S., Yamanishi, Y., 2018. Evaluation of invasiveness by breakdown phenomena of electrically induced bubbles for a needle-free injector. Journal of Microelectromechanical Systems 27, 305–311.

Kitagawa, A., Murai, Y., 2013. Natural convection heat transfer from a vertical heated plate in water with microbubble injection. Chemical Engineering Science 99, 215–224.

Lee, C.H., Choi, H., Jerng, D.W., Kim, D.E., Wongwises, S., Ahn, H.S., 2019. Experimental investigation of microbubble generation in the venturi nozzle. International Journal of Heat and Mass Transfer 136, 1127–1138.

Maeda, Y., Hosokawa, S., Baba, Y., Tomiyama, A., Ito, Y., 2015. Generation mechanism of micro-bubbles in a pressurized dissolution method. Exp. Thermal Fluid Sci. 60, 201–207.

Magnaudet, J., Eames, I., 2000. The Motion of High-Reynolds-Number Bubbles in Inhomogeneous Flows. Annu. Rev. Fluid Mech. 32, 659–708.

Martinez-Bazan, C, Rodriguez-Rodriguez, J., Deane, G.B., Montanes, J.L., Lasheras, J.C., 2010. Considerations on bubble fragmentation models. Journal of Fluid Mechanics 661, 159–177.

Mathai, V., Calzavarini, E., Brons, J., Sun, C., Lohse, D., 2016. Microbubbles and microparticles are not faithful tracers of turbulent acceleration. Phys. Rev. Lett. 117, 024501.

Michaelides, E.E., 1997. Review- the transient equation of motion for particles, bubbles, and droplets. ASME J. Fluids Eng. 119, 233–247.

Murai, Y., 2014. Frictional drag reduction by bubble injection. Exp. Fluids 55, 1773 Article No..

Otsu, N., 1979. A threshold selection method from grey-level histograms. IEEE Transactions on Systems, Man and Cybernetics 9, 62–66.

Park, H.J., Saito, D., Tasaka, Y., Murai, Y., 2019. Color-coded visualization of microbubble clouds interacting with eddies in a spatially developing turbulent boundary layer. Experimental Thermal and Fluid Science 109, 109919.

Plesset, M.S., Prosperetti, A., 1977. Bubble dynamics and cavitation. Annual Rev. Fluid Mechanics 9, 145–185.

Sadatomi, M., Kawahara, A., Kano, K., Ohtmo, A., 2005. Performance of a new microbubble generator with a spherical body in a flowing water tube. Exp. Therm. Fluid Sci. 29, 615–623.

Silva, A.M., Teixeira, J.C.F., Teixeira, S.F.C.F., 2009. Experiments in large scale Venturi scrubber Part II. Droplet size. Chemical Engineering and Processing; Process Intensification 48, 424–431.

Simpson, D.H., Chin, C.T., Burns, P.N., 1999. Pulse inversion Doppler: a new method for detecting nonlinear echoes from microbubble contrast agents. IEEE Transactions on Ultrasonics Ferroelectrics and Frequency Control 46, 372–382.

Sherwood, J.D., 2000. Potential flow around a deforming bubble in a Venturi. International Journal of Multiphase Flow 26, 2005–2047.

Soubiran, J., Sherwood, J.D., 2000. Bubble motion in a potential flow within a Venturi. International Journal of Multiphase Flow 26, 1771–1796.

Sparrow, E., Abraham, J., Minkowycz, W., 2009. Flow separation in a diverging conical duct: Effect of Reynolds number and divergence angle. Int J. Heat Mass Transfer 52, 3079–3083.

Takeda, Y., 2012. Ultrasonic Doppler velocity profiler for fluid flow. Springer Book.

Terasaka, K., Hirabayashi, A., Nishino, T., Fujioka, S., Kobayashi, D., 2011. Development of microbubble aerator for waste water treatment using aerobic activated sludge. Chemical Engineering Science 66, 3172–3179.

Thang, N.T., Davis, M.R., 1981. Pressure distribution in bubbly flow through venturis. Int. J. Multiphase Flow 7, 191–210.

Uesawa, S., Kaneno, A., Nomura, Y., Abe, Y., 2012. Study on bubble breakup behavior in a Venturi tube. Multiphase Science and Technology 24 (3), 257–277.

Usui, S., Sasaki, H., 1978. Zeta potential measurements of bubbles in aqueous surfactant solutions. Journal of Colloid and Interface Science 65, 36–45.

van Wijngaaden, L., 1972. One-dimensional flow of liquids containing small gas bubbles. Annu. Rev. Fluid Mech. 4, 369–395.

Yin, J., Li, J., Li, H, Liu, W., Wang, D., 2015. Experimental study on the bubble generation characteristics for a venturi type bubble generator. Int. J. Heat Mass Transfer 91, 218–224.

Zhao, L., Sun, L., Mo, Z., Tang, J., Hu, L., Bao, J., 2018. An investigation on bubble motion in liquid flowing through a rectangular Venturi channel. Exp. Thermal Fluid Sci. 97, 48–58.

Zhao, L., Sun, L., Mo, Z., Du, M., Huang, J., Bao, J., Tang, J., Xie, G., 2019. Effects of the divergent angle on bubble transportation in a rectangular Venturi channel and its performance in producing fine bubbles. Int. J. Multiphase Flow 114, 192–206.